OCCAM

OXFORD CENTRE FOR COLLABORATIVE APPLIED MATHEMATICS

Capillary deformations of bendable films

by

R.D. Schroll
M. Adda-Bedia
E. Cerda
J. Huang
N. Menon
T.P. Russell
K.B. Toga
D. Vella
B. Davidovitch

OCCAM Preprint Number 13/10

Capillary deformations of bendable films

R.D. Schroll[1,2], M. Adda-Bedia[3], E. Cerda[2], J. Huang[1,4], N. Menon[1],
T.P. Russell[4], K.B. Toga[4], D. Vella[5], and B. Davidovitch[1]
[1] *Physics Department, University of Massachusetts, Amherst MA 01003,*
[2] *Departamento de Física, Universidad de Santiago, Av. Ecuador 3493, Santiago, Chile,*
[3] *Laboratoire de Physique Statistique, Ecole Normale Supérieure, UPMC Paris 06, Université Paris Diderot, CNRS, 24 rue Lhomond, 75005 Paris, France,*
[4] *Department of Polymer Science and Engineering, University of Massachusetts, Amherst MA 01003,*
[5] *Oxford Centre for Collaborative Applied Mathematics, Mathematical Institute, 24-29 St Giles, Oxford OX1 3LB, United Kingdom*
(Dated: February 2, 2013)

We address the partial wetting of liquid drops on ultrathin solid sheets resting on a deformable foundation. Considering the membrane limit of sheets that can relax compression through wrinkling at negligible energetic cost, we revisit the classical theory for the contact of liquid drops on solids. Our calculations and experiments show that the liquid-solid-vapor contact angle is modified from the Young angle, even though the elastic bulk modulus (E) of the sheet is so large that the ratio between the surface tension γ and E is of molecular size. This finding establishes a new type of "soft capillarity" that stems from the bendability of thin elastic bodies rather than from material softness. We also show that the size of the wrinkle pattern that emerges in the sheet is fully predictable, thus resolving a puzzle noticed in several previous attempts to model "drop-on-a-floating-sheet" experiments, and enabling a reliable usage of this setup for the metrology of ultrathin films.

The partial wetting of liquids on solids is among the most basic of capillary phenomena [1]. The fundamental Young's law relates the equilibrium contact angle ϑ_Y of a liquid drop on a solid to the surface energies via

$$\cos\vartheta_Y = (\gamma_{sv} - \gamma_{s\ell})/\gamma \ , \qquad (1)$$

where $\gamma_{sv}, \gamma_{s\ell}$ and $\gamma = \gamma_{\ell v}$ are the mutual surface energies between the solid, vapor, and liquid. This classical equation reflects a balance of forces on the contact line only in the plane of the solid surface and assumes that the normal component of the contact force ($\approx \gamma \sin\vartheta_Y$) induces only slight, localized deformations of the solid substrate that do not affect that balance. However, the normal force balance must be explicitly considered in the partial wetting of soft solids, for which the ratio $\ell_m \equiv \gamma/E$ between surface tension and the Young modulus E of the solid could be a few microns or even more [3–5]. Recent studies that addressed the contact of a liquid drop on semi-infinite soft solids or on soft films of thickness t attached to a stiff substrate [4] showed that the contact angle is no longer determined by a local force balance, and may thus deviate from ϑ_Y. Instead, a minimization of the total energy is required, involving both surface terms and elastic deformations over a characteristic scale, which is the smaller of ℓ_m and t.

A totally different notion of "soft capillarity" is realized when a liquid drop is brought into contact with a stiff thin sheet (*i.e.* ℓ_m is a molecular length) that rests on a soft, easily deformable substrate [2]. Although the sheet's thickness $t \gg \ell_m$, the high deformability of the foundation enables the sheet to respond to the exerted capillary force as a thin elastic body - by bending [6] and developing tangential (in-plane) stresses [7]. Furthermore, it has been realized that for ultrathin sheets, whose thickness is tens of nanometers, in-plane compression relaxes completely through wrinkles whose number diverges as t decreases [8–12]. The "drop-on-a-floating-sheet" experiment (Fig. 1), which provided a systematic study of this *high bendability* regime of partially-wetted sheets, revealed a wrinkle pattern whose size was comparable to the drop's radius R ($0.5 - 1.5$ mm) [7], indicating that the capillary force may affect in-plane stresses and shape deformation on a very large lateral length $\sim R \gg t \gg \ell_m$. An important potential application of this system is the measurement of thickness, surface energy and elastic modulii of ultrathin sheets using only macro-scale features, namely, the extent and number of wrinkles. However, previous studies have failed to provide such a quantitative, predictable link [7, 13].

In this Letter we identify the dimensionless groups that govern soft capillary phenomena and focus on ultrathin, highly-bendable sheets supported by a highly deformable foundation. Our approach employs the compression-free limit of highly-bendable sheets (known as the "membrane limit", "relaxed energy" [10], or "tension field theory" [11]). Two major results of our theory are:

(i) We calculate the stress profile in the sheet, from which we extract the extent of the wrinkled region and compare it with the experimental observations of [7] with no fitting of parameters. Additionally, we present a variant of the original experiment that employs surfactants to manipulate the stress in the sheet. The agreement with our calculations substantiates the validity of our theoretical approach and its usefulness for a precise metrology of thin solid films.

(ii) Our calculations predict that the contact angle between the liquid-vapor and liquid-solid interfaces ($\vartheta + \phi$

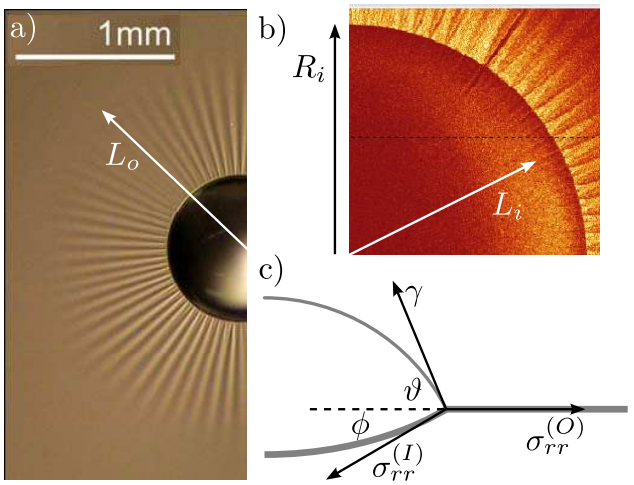

FIG. 1. (a-b) Views of the wrinkle pattern formed by placing a water drop on a floating ultrahin PS sheet ($t = 72\ nm$). The radius of the contact line is R_i. Radial wrinkles appear in: (a) an annular zone $R_i < r < L_O$, and (b) a narrow annulus $L_I < r < R_i$ beneath the drop. Pictures are obtained from confocal slices of a fluorescent sheet [14]. (c) a schematic cross section depicts the forces acting at the contact line (wrinkles are azimuthal undulations around this radial profile).

in Fig. 1c) deviates from ϑ_Y by an amount $\Delta\vartheta$

$$\Delta\vartheta \sim (\ell_m/t)^{1/3} \ , \tag{2}$$

which vanishes rather slowly as $\ell_m/t \to 0$. This prediction indicates that highly-bendable stiff solids on highly-deformable foundations provide a new channel for "soft capillarity" which is distinct from the more familiar case of soft solid films on hard substrates [2–4].

Our system is shown in Fig. 1: A circular elastic sheet of radius R_o, thickness t, and Young modulus E floats on a liquid bath (whose density is ρ) and is pulled taut by the bath-vapor surface tension γ'. A small volume V of liquid of surface tension $\gamma = \gamma_{lv}$ is placed at the center of the sheet. The stretching and bending modulii of the sheet are, respectively, $Y = Et$ and $B = Et^3/12(1-\nu^2)$, where ν is the Poisson ratio. The distinct values of liquid surface tensions ($\gamma' \neq \gamma$) are obtained by adding surfactants to the liquid bath. We define $R(V, \vartheta_Y)$ to be the radius of the contact line on an *undeformed* sheet: $R = (3V/2\pi)^{1/3} \sin\vartheta_Y (1 - 3/2\cos\vartheta_Y + 1/2\cos^3\vartheta_Y)^{-1/3}$. As Fig. 1c shows, the pressure in the drop forces the film to bulge, and hence the radius of the contact line, denoted here by R_i, deviates from R.

The physical parameters can be arranged into six dimensionless groups. The first two are ϑ_Y and γ/γ', which are determined by the surface energies. The second pair of parameters involves the elastic modulii of the sheet:

$$\tilde{\gamma} \equiv \gamma/Y = \ell_m/t \quad ; \quad \epsilon^{-1} \equiv \gamma R^2/B \sim R^2\ell_m/t^3 \ . \tag{3}$$

The parameter ϵ^{-1} quantifies the *bendability* of the sheet [15]. For the ultrathin sheets used in [7] ($t < 300nm$), one finds $\epsilon < 10^{-4}$. In this *high bendability* limit ($\epsilon \ll 1$) the stress in the sheet approaches a compression-free limit [15]. In the high bendability regime, the parameter $\tilde{\gamma}$ dominates the *confinement* in the sheet, namely the sizes of the wrinkled zones on either side of the contact line. Our analysis assumes given values of ϑ_Y and γ/γ', and addresses the behavior for a range of values of $\tilde{\gamma} \ll 1$ (which ensures a Hookean elastic response), assuming the sheet is highly-bendable ($\epsilon \to 0$). In addition to these four dimensionless parameters, the final pair is:

$$\tilde{K} = KR^2/\gamma' \quad ; \quad \tilde{R} = R/R_o \ , \tag{4}$$

where $K = \rho g$. The parameter $\tilde{K}$ quantifies the *deformability* of the liquid foundation, and $\tilde{R}$ is the ratio between the sizes of the drop and the sheet. We address the limit $\tilde{K}, \tilde{R} \to 0$, corresponding to a sufficiently small drop; the effect of $\tilde{K}, \tilde{R} \neq 0$ on the stress is perturbative [15, 16].

Following [13], we consider the inner and outer sides of the contact line, which we denote as (I) and (O), respectively. Beneath the drop, $r < R_i$, the Laplace pressure $P = 2\gamma\sin\vartheta/R_i$ acts downward and causes the sheet to bulge, as depicted in Fig. 1c. The vicinity of the contact line is consequently described by the two angles: ϑ (between the liquid-vapor interface and the horizontal) and ϕ (between the horizontal and the sheet). In the limit $\tilde{\gamma} \to 0$, where the stretching modulus is much larger than the surface tension, the system is expected to approach the classical Young theory where the sheet is undeformed; hence $\vartheta \to \vartheta_Y$ and $\phi \to 0$. Therefore, for $\tilde{\gamma} \ll 1$ the bulge amplitude is small, allowing us to use the Föppl–von Kármán (FvK) framework in which the normal and radial force balance (1^{st} and 2^{nd} FvK) equations approximate the tangents and normal to the sheet through its undeformed (planar) state:

$$(I) \quad \text{radial}: \ d(r\sigma_{rr})/dr - \sigma_{\theta\theta} = 0 \tag{5}$$

$$\text{normal}: \ B\triangle_r^2\zeta - \sigma_{rr}d^2\zeta/dr^2 - \sigma_{\theta\theta}r^{-1}d\zeta/dr = P \tag{6}$$

where $\sigma_{rr}(r), \sigma_{\theta\theta}(r)$ are, respectively, the radial and hoop stress components, $\zeta(r)$ is the normal displacement of the sheet, and $\triangle_r = r^{-1}\frac{d}{dr}(r\frac{d}{dr})$. Outside the contact line, $r > R_i$, only radial force balance need be considered [13]:

$$(O) \quad \text{radial}: \quad d(r\sigma_{rr})/dr - \sigma_{\theta\theta} = 0 \ . \tag{7}$$

The stresses $\sigma_{rr}, \sigma_{\theta\theta}$ in Eqs. (5-7) consist of the elastic stresses and the relevant surface energies [13, 17]. In the high bendability regime, $\epsilon \ll 1$, the bending force in Eq. (6) is negligible with respect to stretching (since $B/R^4 \ll \gamma/R^2$). Hence, we find that each part of the sheet is governed by a single parameter [13, 15, 17, 18]:

$$(O): \ \tau \equiv \sigma_{rr}^{(O)}/\gamma' \ ; \ (I): \ \alpha \equiv Y\gamma^2\sin^2\vartheta/2(\sigma_{rr}^{(I)})^3 \ , \tag{8}$$

where $\sigma_{rr}^{(I)}, \sigma_{rr}^{(O)}$ are, respectively, the radial tensions in the sheet at the inner and outer parts of the contact line (see Fig. 1c), evaluated at $r \to R_i$. The dimensionless α and τ were called *confinement* parameters in [15, 18],

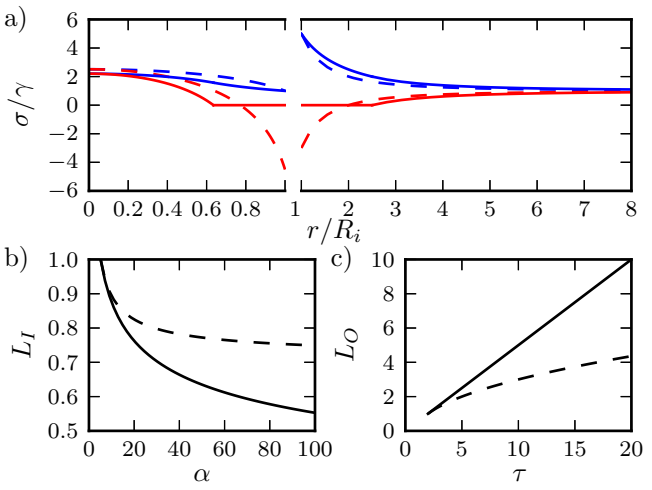

FIG. 2. (a) The stresses σ_{rr} (blue), $\sigma_{\theta\theta}$ (red) beneath the drop ((I), left) and outside the contact line ((O), right) for representative post-threshold values of the confinements: $\alpha = 100$, $\tau = 5$. Solid curves are the compression-free (FT) limit [15, 18]. Dashed curves correspond to the axisymmetric (unwrinkled) state. (b-c) The predictions of both types of stress fields (solid: FT, dashed: axisymmetric state) to the radii of the wrinkled annulus, $L_I(\alpha)$ and $L_O(\tau)$, normalized by R_i.

which addressed simpler set-ups that allowed independent control of α and τ. Those studies showed that by solving Eqs. (5,6) and Eq. (7), the confinement parameters α, τ, together with the angle ϑ, determine completely the elastic stresses and the displacement field in both parts of the sheet, as well as the bulge profile at $r < R_i$. The nature of these solutions will be discussed below; we denote their parametric dependence on α, ϑ, τ by functions: ${u_r}^{(I)}(r;\alpha,\vartheta)$, $\zeta^{(I)}(r;\alpha,\vartheta)$, and ${u_r}^{(O)}(r;\tau)$, with corresponding expressions for the stress components.

In order to find the confinements α, τ and the angle ϑ, we must consider the vicinity of the contact line. First we note that the bulge's shape, $\zeta^{(I)}(r;\alpha,\vartheta)$, allows us to express the radius R_i and the angle ϕ as functions of the drop's volume V and the unknown α, ϑ. Next, we obtain two equations from the continuity of the shape and the force balance (in $\hat{r}$) at the contact line $r \to R_i$ [19]:

$$u_r^{(I)} = u_r^{(O)} \ , \tag{9}$$

$$\sigma_{rr}^{(I)} \cos\phi + \gamma \cos\vartheta = \ \sigma_{rr}^{(O)}, \tag{10}$$

The system (9,10) provides two equations for the three unknowns: α, τ and ϑ, indicating that another physical mechanism beyond local force balance at the contact line is required. Following [2], we find the missing relation by minimizing the total energy U_T, consisting of the elastic energy of the deformed sheet and the surface energies of the sheet, drop, and bath.

Let us turn now to the solution of Eqs. (5,6,7) for some given parameters α, ϑ [18] and τ [15]. An obvious solution of these equations is the axisymmetric state, whose displacement field and corresponding stress are given in [17]. Below critical values ($\alpha_c \approx 5.16$ [18], $\tau_c = 2$ [20]), the axisymmetric solution of the problem is purely tensile (*i.e.* both $\sigma_{rr}^{(axi)}$ and $\sigma_{\theta\theta}^{(axi)}$ are positive everywhere). However, beyond these critical values, the axisymmetric state develops azimuthal (hoop) compression ($\sigma_{\theta\theta}^{(axi)}(r) < 0$) in annuli $L_I(\alpha) < r < R_i$ and $R_i < r < L_O(\tau)$, respectively (Fig. 2); signaling the emergence of radial wrinkles. For post-threshold confinement values, traditional post-buckling methods use the axisymmetric state to approximate the stress of the wrinkled state [13, 20]. However, it has been realized that in the high bendability regime, $\epsilon \ll 1$, where only tiny level of compression can be accommodated, this "near threshold" approach must be replaced by a *far from threshold* (FT) singular perturbation theory around the compression-free "membrane limit" that satisfies $\sigma_{\theta\theta} \geq 0$ as $\epsilon \to 0$. For a given $\alpha > \alpha_c$ ($\tau > \tau_c$), the compression-free stress that characterizes the wrinkled state is substantially different from the compressive stress field of the axisymmetric state (Fig. 2). In [17] we give the FT results for the displacement field and the compression-free stress. In the post-threshold regime (*i.e.* if $\alpha > \alpha_c$, $\tau > \tau_c$), the FT results must be used in our matching analysis, Eqs. (9,10).

Fig. 3 presents the results of our calculation. In order to compare with the experiment, we set $\vartheta_Y = \pi/2$ (the contact angle of a water drop on a polystyrene surface) and present results for several values of $1/3 \leq \gamma'/\gamma \leq 3$ (results for $\vartheta_Y \neq \pi/2$ are qualitatively similar [17]). In Fig. 3a-3b we show the computed values of the confinement parameters α and τ as functions of $\tilde{\gamma} = \gamma/Y$. The experiments are performed with $1/2 \leq \gamma'/\gamma \leq 1$ and a range of thicknesses ($30\ nm \leq t \leq 300\ nm$) for which $\tilde{\gamma} < 10^{-2}$, such that the predicted values of α, τ are beyond threshold and a wrinkle pattern is expected. Fig. 3c shows the deviation $\Delta\vartheta$ of the angle $\vartheta + \phi$ (between the sheet and the liquid-vapor surface) from ϑ_Y. Notably, the deviation scales as $\Delta\vartheta \sim \tilde{\gamma}^{1/3}$. Another interesting result is shown in Fig. 3d: As $\tilde{\gamma} \to 0$ the deviation $\Delta\vartheta$ is equally divided between ϕ and $\vartheta - \vartheta_Y$. These two results are confirmed by an asymptotic analysis [17].

Figures 4a,b compare the measured extent of the wrinkled zone outside the drop with the calculated $L_O(\tau)$ from the predicted values of $\tau(\tilde{\gamma})$. In Fig. 4a (data reproduced from [7]), the thickness t varies (hence changing $\tilde{\gamma}$), whereas in Fig 4b we vary the surfactant concentration in the bath, thus changing γ'/γ. The predictions based on the FT wrinkling theory, free of any fitting paramaters, are in good agreement with the experimental data. The predicted profile below the drop ($\zeta(r)$ for $r < R_i$) overestimates the measured one (Fig. 4c). Despite this slight disagreement, our measurements of the angle deviation $\Delta\vartheta$ (Fig. 3c), taken from two different setups [14] agree with the predicted scaling, Eq. (2). This analysis substantiates the validity of the FT approach and calls for its usage in metrological methods that extract material parameters of ultrathin films from wrinkle patterns [7].

Beyond the specific regime addressed in this Letter, the four dimensionless parameters defined in Eqs. (3,4)

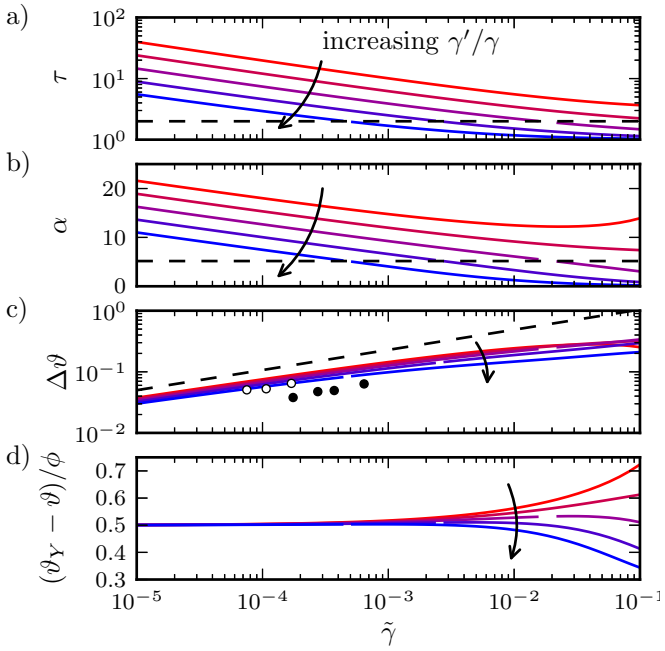

FIG. 3. (a-b) Computed values of α, τ for $10^{-5} < \tilde{\gamma} < 10^{-1}$. Here $\vartheta_Y = \pi/2$ and colors correspond to several values of γ'/γ between 0.33 (red) and 3 (blue). For sufficiently large $\tilde{\gamma}$, the (unwrinkled) axisymmetric state is stable since $\alpha(\tilde{\gamma}) < \alpha_c, \tau(\tilde{\gamma}) < \tau_c$. As $\tilde{\gamma}$ decreases, $\alpha(\tilde{\gamma})$ and $\tau(\tilde{\gamma})$ exceed the critical values and the wrinkled state of the highly-bendable sheet ($\epsilon \to 0$) is described by the FT theory. (c) A log-log plot of the computed difference $\Delta\vartheta$ of the angle $\vartheta + \phi$ (between the liquid-vapor interface and the sheet) from ϑ_Y. Dashed line (guide to the eye) has a slope 1/3. The solid circles taken from confocal fluorescence microscopy measurements of the profile of the sheet under the drop, as in Fig. 1. The open circles are from a different, but comparable configuration [14]. Data points are the measured angle ϕ divided by 2 (using the asymptotic result $\phi \approx 2\Delta\vartheta$). Error bars are comparable to the circle size. (d) The ratio $(\vartheta_Y - \vartheta)/\phi \to 1/2$ as $\tilde{\gamma} \to 0$.

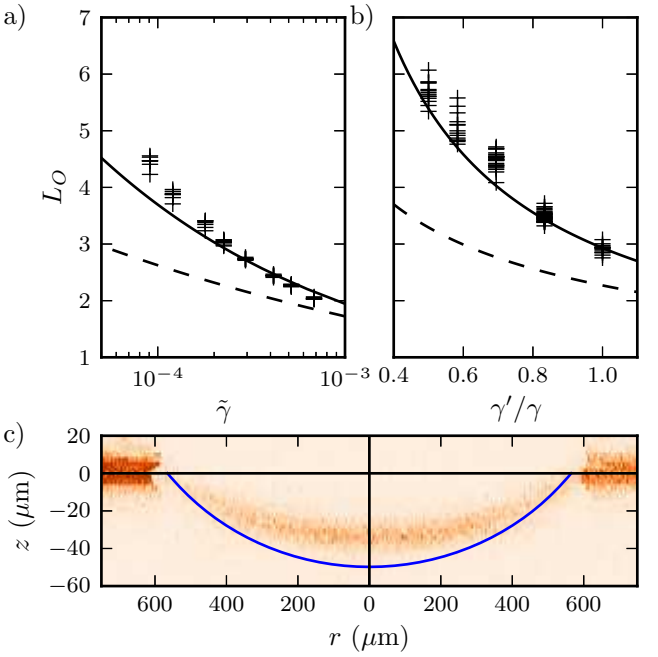

FIG. 4. (a-b) Comparison between the observed and predicted outer radius, $L_O(\tau)$, of the wrinkled annulus (normalized by R_i). Solid curve: prediction of the FT theory. Dashed curve: prediction based on approximating the stress through the axisymmetric state [13]. In 4a, $\gamma = \gamma' = 72$ *dyn/cm* and $\tilde{\gamma}$ varies (data obtained by varying the sheet's thickness t from 31 to 233 *nm* [7]). In 4b the thickness is $t = 94$ *nm* and γ'/γ ranges from 0.5 to 1 due to surfactant added to the liquid bath. (c) The measured profile beneath the drop, obtained by confocal microscopy [14] and the predicted profile (blue).

constitute a universal framework for classifying distinct types of soft capillary phenomena. Following [12], we generalize the physical parameter K in Eq. (4) to reflect the effective stiffness of the foundation. For the particular case of an elastic substrate of Young modulus E_s, $K \approx E_s/R$ (where R is the characteristic deformation scale), and hence the deformability $\tilde{K}^{-1} \approx \gamma/RE_s$. Refs. [2, 4] addressed soft films, $t \ll \ell_m$ ($\tilde{\gamma} \ll 1$) on undeformable substrates $\tilde{K} \gg 1$, and found that the film deforms as a 3D body in a region of size t around the contact line. The case addressed in this Letter, of a stiff thin film ($\ell_m \ll t \ll R$) on a highly deformable foundation ($\tilde{K} \ll 1$), exhibits a completely different behavior, where the sheet responds to the capillary forces as a thin body, through bending and in-plane stresses [2]. Here we focused on the high-bendability regime ($\epsilon \ll 1$) where the stress approaches a compression-free limit, but a different low-bendability behavior ($\epsilon \lesssim 1$) may be expected for thicker sheets [6] for which large bending forces can balance compression in the sheet. In addition to bendability values, another crucial difference between our work and that of [6] is encoded in the ratio $\tilde{R} = R/R_o$ between the drop and the sheet. In contrast to [6], we addressed the case $\tilde{R} \ll 1$ (more precisely $\tilde{K}\tilde{R}^{-2} \gg 1$), such that a response in which the whole sheet rolls over the drop, thus making a developable stress-free shape, is impossible. We hope that future work will explore soft capillary phenomena in different regimes of this parameter space.

ACKNOWLEDGMENTS

We acknowledge support by the Petroleum Research Fund of the American Chemical Society (RDS, BD), NSF-MRSEC on Polymers at UMass Amherst DMR 08-20506 (RDS, JH, KBT), Fondecyt project 3120228 (RDS) and 1095112 (EC), Anillo Act 95 (EC), the Department of Energy Office of Basic Energy Sciences ER45612 (JH, KBT, TPR), NSF DMR 09-07245 and DMR 12-0778 (NM), a grant KUK-C1-013-04 made by King Abdullah University of Science and Technology (DV), NSF CAREER award DMR 11-51780 (BD).

[1] P.G. De Gennes, F. Brochard-Wyart, and D. Quere, *Capillarity and Wetting Phenomena: Drops, Bubbles, Pearls, Waves*, Springer (2003).

[2] J. Olives, J. Phys. Cond. Mat. **5** 2081 (1993); J. Olives, SIAM J. App. Math. **56**, 480 (1996).

[3] M.E.R. Shanahan, J. Adhes. **18**, 247 (1985).

[4] E.R. Jerison, Y. Xu, L. A. Wilen, and E. R. Dufresne, Phys. Rev. Lett. **106**, 186103 (2011).

[5] R.W. Style and E.R. Dufresne, Soft Matter **8**, 7177 (2012).

[6] C. Py *et al.* Phys. Rev. Lett. **98**, 156103 (2007).

[7] J. Huang *et al.*, Science **317**, 650 (2007).

[8] H. Wagner, Z. Flug. Motor. **20**, 8 (1929).

[9] M. Stein and J.M. Hedgepeth, NASA Technical Note D-813 (1961).

[10] A.C. Pipkin, IMA J. App. Math. **36**, 85 (1986).

[11] E.H. Mansfield, *The Bending and Stretching of Plates*, (Cambridge University Press, Cambridge, 1989).

[12] E. Cerda and L. Mahadevan, Phys. Rev. Lett. **90**, 074302 (2003).

[13] D. Vella, M. Adda-Bedia and E. Cerda, Soft Matter **6**, 5778 (2010).

[14] K.B. Toga, T.P. Russell and N. Menon, submitted to Soft Matter.

[15] B. Davidovitch *et al.*, Proc. Nat. Acad. Sci. **108**, 18227 (2011).

[16] J. Huang *et al.*, Phys. Rev. Lett. **105**, 038302 (2010).

[17] See supplementary material

[18] H. King, R.D. Schroll, B. Davidovitch and N. Menon, Proc. Nat. Aca. Sci. **109**, 9716 (2012).

[19] In [17] we show that continuity and force balance in $\hat{\zeta}$ are automatically satisfied.

[20] S.P. Timoshenko and J.N. Goodier, *Theory of Elasticity*, (McGraw Hill, New York, 1961).

RECENT REPORTS

12/102	A New Lattice Boltzmann Equation to Simulate Density-Driven Convection of Carbon Dioxide	Allen Reis Sun
12/103	Control and optimization of solute transport in a porous tube	Griffiths Howell Shipley
12/104	Air-cushioning in impact problems	Moore Ockendon Oliver
12/105	Strain controlled biaxial stretch: An experimental characterization of natural rubber	Pancheri Dorfmann
12/106	Non-linear modeling of active biohybrid materials	Paetsch Dorfmann
12/107	Coalescence of Liquid Drops: Different Models Versus Experiment	Sprittles Shikhmurzaev
12/108	Adjoint Based A Posteriori Analysis of Multiscale Mortar Discretizations with Multinumerics	Tavener Wildey
12/109	Dynamics of mechanically induced fiber reorientation in the material reinforced by two families of fibers	Melnik Goriely
12/110	Multiscale stochastic reaction-diffusion modelling: application to actin dynamics in filopodia	Erban Flegg Papoian
12/111	Exploiting the Synergy Between Carboplatin and ABT-737 in the Treatment of Ovarian Carcinomas	Jain Richardson Meyer-Hermann Byrne
12/112	The integration of hormonal signaling networks and mobile microRNAs is required for vascular patterning in Arabidopsis roots	Muraro Pound Help Lucas Chopard Byrne Godin Hodgman King Pridmore Helariutta Bennett Bishopp
12/113	Fast solution of Cahn-Hilliard Variational Inequalities using Implicit Time Discretization and Finite Elements	Bosch Stoll Benner
12/114	An Embedding Technique for the Solution of Reaction-Diffusion Equations on Algebraic Surfaces with Isolated Singularities	Rockstroh März Ruuth

13/01	Rotation, inversion, and perversion in anisotropic elastic cylindrical tubes and membranes	Goriely Tabor
13/02	Drop spreading and penetration into pre-wetted powders	Marston Sprittles Zhu Li Vakarelski Thoroddsen
13/03	On the mechanics of thin films and growing surfaces	Holland Kosmata Goriely Kuhl
13/04	Spatially Partitioned Embedded Runge-Kutta Methods	Ketcheson Macdonald Ruuth
13/05	Simple computation of reaction-diffusion processes on point clouds	Macdonald Merriman Ruuth
13/06	A Volume-Based Method for Denoising on Curved Surfaces	Biddle von Glehn Macdonald März
13/07	Porous squeeze-film flow	Knox Wilson Duffy McKee
13/08	Diffusion of finite-size particles in confined geometries	Bruna Chapman
13/09	Mathematical analysis of a model for the growth of the bovine corpus luteum	Prokopiou Byrne Jeffrey Robinson Mann Owen

Copies of these, and any other OCCAM reports can be obtained from:

Oxford Centre for Collaborative Applied Mathematics
Mathematical Institute
24 - 29 St Giles'
Oxford

OX1 3LB
England
www.maths.ox.ac.uk/occam